A method for pole figure measurements via a dynamic segmented spiral scheme

Surya Chandramouleeswaran, Adam Creuziger and Kip Findley

IUCr Journals
CRYSTALLOGRAPHY JOURNALS ONLINE

A method for pole figure measurements via a dynamic segmented spiral scheme

Surya Chandramouleeswaran,[a,b] Adam Creuziger[c]* and Kip Findley[b]

[a]BASIS Chandler High School, 4825 South Arizona Avenue, Chandler, AZ 85248, USA, [b]Metallurgical and Materials Engineering Department, Colorado School of Mines, 1301 19th Street, Hill Hall, Golden, CO 80401, USA, and [c]Materials Science and Engineering Division, National Institute of Standards and Technology, 100 Bureau, Gaithersburg, MD 20899, USA. *Correspondence e-mail: adam.creuziger@nist.gov

A new method for pole figure measurement is described, entitled a dynamic segmented spiral scheme. Compared with the schemes currently in use, the dynamically segmented spiral scheme is shown to have advantages in terms of evenness of pole figure coverage and phase fraction accuracy. The phase fraction accuracy is shown to be robust for a variety of texture components commonly encountered in steels and for texture sharpness exceeding what is commonly encountered for rolled sheet steels. This scheme provides a promising alternative to conventional methods of simultaneous texture and phase fraction measurement.

1. Background

Many engineering materials make use of multiple crystalline phases to produce properties that are an improvement upon what can be achieved by a single phase. Recent advances in materials science have enabled the development of several classes of materials that take advantage of effects introduced by additional phases, one example of which is provided by third-generation advanced high strength steels (Han *et al.*, 2009; De Moor *et al.*, 2010; Abu-Farha *et al.*, 2018). In addition to phase fraction information, crystallographic texture is another key parameter to quantify, as the processing, production, use and failure modes may depend on the arrangement of the microstructure. Therefore accurate measurement of both the phase fraction and texture is often key for the verification of material design and prediction of material behavior.

A common method for collecting and displaying crystallographic texture data is the use of pole figures (Bunge, 1982; Kocks *et al.*, 1998). These are a stereographic representation of intensity variations in a material, plotted for a particular *hkl* plane as a function of sample orientation. Sample orientation vectors for rolled sheets are often expressed in terms of the rolling direction (RD), transverse direction (TD) and normal direction (ND). Pole figures are typically collected by moving the sample through a series of rotations and *hkl* planes. A more complete representation of crystallographic texture, termed an orientation distribution function (ODF), can be calculated using data from several pole figures through pole figure inversion techniques: spherical harmonics (Bunge, 1982; Roe, 1965), WIMV (Matthies & Vinel, 1982), EWIMV (Lutterotti *et al.*, 2004) and summation of radially symmetric functions (Hielscher & Schaeben, 2008). These pole figure inversion techniques have been implemented in *PopLA* (Kallend *et al.*, 1991), *BEARTEX* (Wenk *et al.*, 1998), *MAUD* (Lutterotti, 2000) and *mtex* (Hielscher & Schaeben, 2008).
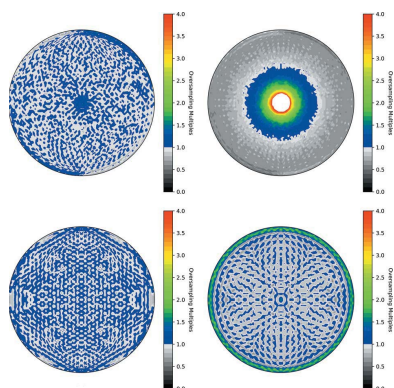
Numerous laboratory diffraction instruments, synchrotron X-ray beamlines and neutron beamlines can provide phase fraction and crystallographic texture measurements. Data from these instruments can often be used to measure simultaneously both phase fractions and crystallographic texture. As many advanced materials use metastable phases, the traditional approach of powdering a sample will result in inaccurate phase measurements, as some portion of the sample may transform into other phases. Phase fraction and stability are often functions of composition and processing, necessitating measurements on the material as produced. When diffraction data are recorded, the phase fraction data are often calculated from a simple summation (Jatczak *et al.*, 1980; Creuziger *et al.*, 2021) over all diffraction vectors (*i.e.* positions on a pole figure) measured. However, as shown by Creuziger *et al.* (2021, 2018*a*), summation alone can lead to bias in the phase fraction. Bias errors were found to be negligible when a series of diffraction vectors were evenly distributed over a pole figure. Phase measurements that take the texture of the sample into account, either by simultaneously fitting the texture and phase fraction (co-refinement) (Wenk *et al.*, 2003; Matthies *et al.*, 2005; Larson & Dreele, 2004; Toby & Von Dreele, 2013) or by even measurement of the pole figure (Creuziger *et al.*, 2018*a*), should be more accurate.

Co-refinement algorithms applied to diffraction data typically rely on two alternating fitting sequences: first a fit of the texture, and second a propagation of the texture values to each diffraction peak to modify the intensity as a function of the relative sample orientation. This technique has been routinely applied for several time-of-flight (TOF) neutron sources such as HIPPO (Wenk *et al.*, 2010), iMATERIA (Onuki *et al.*, 2020), TAKUMI (Xu *et al.*, 2018) and NOMAD (Peterson *et al.*, 2021). As shown for a limestone sample investigated as part of a round robin (Wenk, 1991; Lutterotti *et al.*, 1997), it is possible to get consistent texture data from the co-refinement approach.

By contrast, the phase fraction accuracy of the co-refinement technique has not been studied as extensively. As noted in several quantitative phase analysis round robins involving Rietveld refinement that do not add the additional complexity of texture effects (powdered materials), significant deviations can occur due to choices made by the operator (Madsen *et al.*, 2001; Fawcett *et al.*, 2010). The large number of variables (Fawcett *et al.*, 2010), the dependence of accuracy on converged parameters across all data sets (Vogel *et al.*, 2018), the complex procedure (Wenk *et al.*, 2010) and the effect of order of refinement (Rowles, 2021) have each been identified as contributing factors in these deviations. One advantage of complete and even pole figure measurement techniques to determine phase fraction is that the bias errors due to texture are accounted for without requiring Rietveld refinement. However, a disadvantage of the complete pole figure technique is that the number of peaks measured is typically lower, which can introduce other errors in phase fraction measurements.

Electron backscatter diffraction (EBSD) is another technique that is routinely used for texture and phase fraction measurements (Schwartz *et al.*, 2009). This technique typically provides a spatial map of the phases and orientations present on a prepared surface. While growing in usage, there are a number of challenges for accurate measurements. For texture measurements, the number of grains required for accuracy is estimated to be 10 000 (Wright *et al.*, 2007). The data sets and time required for each scan grow rapidly if the suggested number of EBSD points per grain for grain size measurements (>100; International Organization for Standardization, 2020) are recorded. Wright *et al.* (2007) noted that differences in grain size between phases can cause additional challenges. The step size and data cleaning choices are also likely to have an impact on the accuracy of the measurements, particularly if the phases have different grain sizes or shapes.

A series of diffraction vectors for texture measurements via pole figures has been termed a sampling scheme by Kocks *et al.* (1998), and their work also includes some examples. A well known sampling scheme is the equal angle grid, where the diffraction vectors are arranged in an even grid of angles (often with 5° resolution). As noted by Kocks *et al.* (1998), these equal angle grids result in an uneven distribution of pole figure area coverage. The hexagonal grids of Matthies (Matthies & Wenk, 1992) and Rizzie (2008) were developed to address the problem of uneven area coverage. These grids have an additional benefit in that, for a given sampling scheme resolution, they reduce the number of measurement points compared with an equal angle grid.

Prior to the use and development of equal angle and hexagonal sampling schemes, spiral sampling schemes were developed. As shown in some of the original work by Holden (1953) and included in the book by Klug & Alexander (1974), these early spiral schemes were accomplished by mechanical linkages between the tilt and rotation motors. This arrangement results in a spiral that has a constant rate of expansion (*i.e.* an Archimedean spiral). While computer control of the X-ray goniometer stage has made mechanical linkages obsolete and therefore spiral techniques have fallen out of use, spiral schemes have the advantage of allowing continuous motion of the sample. However, the use of a mechanical linkage for a spiral scheme (or reproduction via computer control) will probably result in uneven pole figure area coverage, similar to the equal angle grid demonstrated by Kocks *et al.* (1998).

This paper demonstrates a new spiral scheme with even pole figure area coverage, termed a dynamic segmented spiral (DSS). The DSS scheme was developed to cover the pole figure space more evenly, with the hypothesis that more even coverage will provide a more accurate phase fraction and texture measurement than other sampling schemes. The spiral motion also allows for simple summation and continuous motion, unlike more discrete schemes.

2. Methods

To eliminate additional sources of variation inherent in experimental data and analysis methods, this work uses simulated texture and phase data, as done by Creuziger *et al.*
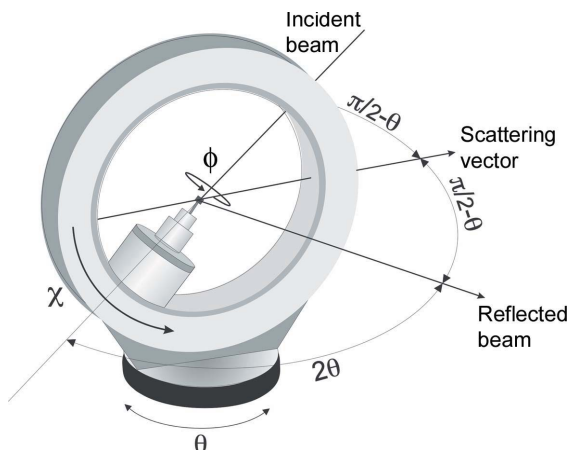
Figure 1
A sketch of a goniometer for pole figure measurements in transmission geometry, with rotation (ϕ) and tilt (χ) axes labeled. The Bragg angle (θ) is also shown, but is not considered in this work. Courtesy of Thomas Gnäupel-Herold.

(2018a). In order to achieve complete pole figure coverage, the sampling schemes explored here assume a transmission geometry. Fig. 1 is an illustration of a goniometer and the angle conventions used for neutron diffraction. The effects of incomplete pole figure coverage and intensity corrections from sample tilt, such as are commonly encountered in reflection geometry, are outside the scope of this work.

Four different sampling schemes were explored, the new DSS scheme, the hexagonal grids of Matthies and Rizzie, and the Holden spiral scheme. The number and distribution of diffraction vectors are compared between the four sampling schemes, together with ODF accuracy and accuracy of the phase fraction by summation. For comparison, a common resolution parameter (ζ) was used in the construction of each sampling scheme. The code base developed by Creuziger *et al.* (2018a) was built upon in this work, with observations on even pole figure coverage from Creuziger *et al.* (2021) used to inform the DSS scheme. The code used for this work is available at https://github.com/usnistgov/Texture-Sampling-PhaseMeasurement-BiasErrors as release 2.2.0.

2.1. Definition of the DSS

To create a spiral with even pole figure area coverage, the pole figure sphere is divided into discrete spherical segments. As shown by Creuziger *et al.* (2021), spherical segments provide a simple calculation for spherical area. The polar angle between each pair of adjacent segments is defined by a resolution parameter (ζ). The spiral scheme iterates through a full goniometer rotation ($0 < \phi \leq 360°$) while the range of the goniometer tilt (χ) is limited within the range of each spherical segment. The initial point of the spiral is set at $\chi_0 = 90°$ and $\phi_0 = 0°$. The next step in the spiral is determined by equations (1)–(5):

$$p = \frac{360°}{\zeta} \sin(\chi_{n-1}), \tag{1}$$

$$\phi_s = \frac{360°}{p}, \tag{2}$$

$$\chi_s = \frac{\zeta}{p}, \tag{3}$$

$$\phi_n = \phi_{n-1} + \phi_s, \tag{4}$$

$$\chi_n = \chi_{n-1} - \chi_s. \tag{5}$$

The step increments ϕ_s and χ_s are updated on the basis of the prior χ value. Any additional rotation beyond $\phi > 360°$ is also retained in this method when moving to the next spherical segment. The tilt increment value is therefore small at the start of the spiral and increases continuously towards the center of the pole figure. This spiral scheme is termed a dynamic segmented spiral (DSS) in the rest of this work.

2.1.1. Holden spiral. The construction of the Holden spiral uses a constant rate of rotation for ϕ and a scaled rate of rotation for χ. The rate of expansion of the Holden spiral is set by the same resolution parameter (ζ) as is used in the DSS. Using the initial point $\phi_0 = 0°$ and for $\phi_n \leq 360°(90°/\zeta)$, the Holden spiral is defined by equations (6) and (7):

$$\phi_n = \phi_{n-1} + \zeta, \tag{6}$$

$$\chi_n = \phi_n \frac{\zeta}{360°}. \tag{7}$$

2.1.2. Rizzie hexagonal grid. The construction of the Rizzie hexagonal grid described in equations (8)–(18) is largely identical to the description given by Rizzie (2008), where a mesh of equilateral triangles is placed over an equal area pole figure. However, stereographic conversions for equal area (Kocks *et al.*, 1998) are now explicitly added [replacing R in the work of Rizzie (2008) with D_{max} here]. χ_{max} was set equal to 90°. The resolution parameter (ζ) is used to determine the value of N,

$$N = \frac{90°}{\zeta}. \tag{8}$$

The maximum value of tilt is converted to a D_{max} value using the equation for an equal area stereographic projection,

$$D_{max} = 2 \sin(\chi_{max}/2). \tag{9}$$

To construct the grid, an integer series j is used, with

$$j = \{0, 1, 2, \ldots\} \tag{10}$$

and a constructor function y_j defined as

$$y_j = j \frac{(3^{1/2}) D_{max}}{2N}. \tag{11}$$

The values for j are limited by the inequality

$$|y_j| \leq D_{max}. \tag{12}$$

A second integer series i takes values within the inequality,

$$i \frac{D_{max}}{N} \leq \left[(D_{max})^2 - (y_j)^2 \right]^{1/2}. \tag{13}$$

The constructor function x_{ij} takes the following values:

$$x_{ij} = \begin{cases} (D_{\max}/N)\, i & \text{if } j \bmod 2 = 0, \\ (D_{\max}/2N) + (D_{\max}/N)\, i & \text{if } j \bmod 2 = 1. \end{cases} \quad (14)$$

The constructor functions are then used to calculate the tilt with an intermediate step,

$$D_{ij} = \left[(x_{ij})^2 + (y_j)^2 \right]^{1/2}, \quad (15)$$

before using the inverse stereographic function to determine the tilt position χ_{ij},

$$\chi_{ij} = 2 \arcsin \left(\frac{D_{ij}}{2} \right). \quad (16)$$

The rotation positions for the first and second quadrants of the pole figure are found from

$$\phi_{ij} = \begin{cases} \arctan(y_j/x_{ij}) & \text{if } x_{ij} > 0, \\ 90° & \text{if } x_{ij} = 0, \\ \arctan(y_j/x_{ij}) + 180° & \text{if } x_{ij} < 0, \end{cases} \quad (17)$$

while the rotation positions for the third and fourth quadrants are found from

$$\phi_{ij} = \begin{cases} \arctan(y_j/x_{ij}) + 180° & \text{if } x_{ij} > 0, \\ 270° & \text{if } x_{ij} = 0, \\ \arctan(y_j x_{ij}) + 360° & \text{if } x_{ij} < 0. \end{cases} \quad (18)$$

2.1.3. Matthies hexagonal grid. The Matthies hexagonal grid is based on hexagonal tiles covering a pole figure, but is implemented as a series of concentric rings. The original reference for the Matthies hexagonal grid (Matthies & Wenk, 1992) does not include an explicit algorithm for how to construct the grid. However, this grid is implemented at the National Institute of Standards and Technology (NIST) Center for Neutron Research (NCNR) on the Residual Stress Diffractometer (Brand *et al.*, 1997) and the algorithm was provided to the present authors. ζ is a resolution parameter as described above. In this case, the discretization occurs in the rotation n_ϕ and is described in equations (19)–(23).

$$n_\phi = \left\lfloor \frac{360°}{\zeta} \right\rfloor, \quad (19)$$

where $\lfloor \rfloor$ indicates rounding to the nearest whole number. Similarly to the Rizzie hexagonal grid, two integer series are used in the grid construction, limited by the inequality $6i \leq n_\phi$ for i,

$$i = \left\{ 0, 1, 2, \ldots, \frac{n_\phi}{6} \right\}, \quad (20)$$

and limited by the inequality $j \leq n_\phi - 6i$ for j,

$$j = \{ 1, 2, \ldots, (n_\phi - 6i) \}. \quad (21)$$

The tilt and rotation positions are then set by

$$\phi_{ij} = \frac{360°}{n_\phi - 6i} (j - 1), \quad (22)$$

$$\chi_{ij} = 2 \arcsin \left[\frac{2^{1/2}}{2} \frac{(n_\phi/6) - i}{(n_\phi/6)} \right]. \quad (23)$$

While it is possible to move the sample continuously along a spiral path, for our comparison with other sampling schemes a discrete approach was used. The time required to traverse each spiral was divided into equal increments, and the diffraction vector position at each increment was determined for both the DSS and the Holden spiral. Discretization also permits a calculation for the 'number of points' as measured by the spiral schemes for comparison with the hexagonal grids. Experimentally, the total measurement time is expected to be a multiple of the number of points measured. In this work the additional time required for motor motion is not directly discussed, but the motor motion time is expected to correlate with the number of points measured. The code for each of these equations has been implemented in the program at https://github.com/usnistgov/Texture-Sampling-Phase Measurement-BiasErrors (Creuziger *et al.*, 2018*b*) and is available there for reference or use.

2.2. Sampling scheme comparison

To compare the evenness of pole figure area coverage, oversampling plots were created using the density contour function in the *mplstereonet* package (Kington, 2015). This function discretizes the pole figure into small areas (each approximately 1% of the total hemisphere area) and computes the number of points inside each area (option 'Schmidt' in *mplstereonet*). The number of points per area is then normalized and depicted as a filled contour function. The values of the contour function represent the density of points, which is equivalent to the number of times a particular area is oversampled (values > 1), undersampled (values < 1) or evenly sampled (= 1).

To compare the distribution of diffraction vectors, histograms of the closest adjacent vector were calculated. A matrix of dot products for each vector series was computed and sorted by value, and the second term was retained (as the first term corresponds to 0, the vector dotted with itself). These histograms are expressed as a relative probability for comparison.

2.3. ODF accuracy

Following the work described by Creuziger *et al.* (2021, 2018*a*), 20 common texture components for rolled steel sheets were used to assess the accuracy of the ODFs. These texture components are separated into seven face-centered cubic components for the austenite (γ) phase and 13 body-centered cubic components for the ferrite (α) phase. These components are commonly encountered during rolling processes (Dillamore & Roberts, 1964; Bleck *et al.*, 1991; Kocks *et al.*, 1998; Kestens & Jonas, 2005) and were implemented via the texture analysis package *mtex* (Hielscher & Schaeben, 2008) with cubic crystal symmetry and orthotropic sample symmetry.

An ODF for each texture component was created and pole figures using each of the four sampling schemes were

calculated. Pole figures for the *hkl* planes (111), (200) and (220) for the austenite phase and the (110), (200) and (211) planes for the ferrite phase were chosen for this work. Using these pole figures as input, a recalculated ODF was created. The difference between the original ODF and the recalculated ODF was determined, and the mean difference was calculated for each texture component. For this analysis, the pole figure resolution parameter ζ was fixed at 5°, and the half-width of the recalculated ODF was also fixed at 5° to match the pole figure resolution.

The sharpness of individual texture components was also investigated. Texture sharpness was implemented by assigning variable half-width values to each of the individual texture components to create an orientation distribution function (ODF). A half-width range from 2.5 to 50° was analyzed in this work.

2.4. Phase fraction accuracy with textured data

As discussed previously by Creuziger *et al.* (2021, 2018*a*), crystallographic texture and oversampling can affect phase fraction measurements. The common ODF components listed in the previous section were also used to assess the accuracy of phase fractions determined by summation.

The phase fraction calculations follow the equations laid out by Creuziger *et al.* (2021). ODFs were used to calculate pole figures for a selection of *hkl* planes. Pole figure normalized intensity values $\hat{I}^{hkl}(\phi, \chi)$ for each *hkl* were extracted from these pole figures. Note that this intensity normalization is not the same as traditional normalization by the theoretical intensities but is solely based on texture and sampling effects. The pole figure normalized intensity bypasses sources of variation other than the sampling scheme and crystallographic texture. Interpolated values were used when the required (ϕ, χ) values were not coincident with the original pole figure grid. These pole figure normalized intensity values are given in terms of multiples of a uniform (or random) distribution. To investigate the bias errors in the phase fraction measurement, a known phase fraction was imposed on the data. In this work an austenite phase fraction (ξ) of 0.25 and ferrite phase fraction of 0.75 $(1 - \xi)$ were used, matching the values assumed by Creuziger *et al.* (2018*a*). The austenite phase fraction V_γ is calculated from a rule of mixtures,

$$V_\gamma = \frac{\xi \hat{I}_\gamma}{\xi \hat{I}_\gamma + (1 - \xi) \hat{I}_\alpha}, \tag{24}$$

where $\hat{I}_\gamma$ and $\hat{I}_\alpha$ are the average of all $\hat{I}^{hkl}(\phi, \chi)$ values measured for each phase.

As with the ODF reconstruction, the particular *hkl* planes used to calculate the phase fraction can affect the accuracy of phase fraction measurement (Creuziger *et al.*, 2021, 2018*a*). Common approaches include using intensity data from a select list of measured peaks or fitting the entire spectrum of data (*i.e.* Rietveld refinement). Evaluating the question of which particular peak choice selections are optimal was outside the scope of this project. The *hkl* planes (111), (200) and (220) for the austenite phase and the (110), (200) and (211) planes for

Table 1
A summary of the number of sampling points for each tested scheme resolution.

Scheme resolution	DSS	Holden	Rizzie	Matthies
2.5°	3303	5185	3805	1801
5.0°	828	1297	955	469
10.0°	209	325	241	127

the ferrite phase were chosen as benchmarks for this work, as in the ODF reconstruction.

3. Results

3.1. Comparison of sampling schemes

A discrete representation of the DSS scheme is shown Fig. 2(*a*). Discrete representations of the spiral scheme of Holden [Fig. 2(*b*)], the hexagonal grid of Rizzie [Fig. 2(*c*)] and the hexagonal grid of Matthies [Fig. 2(*d*)] are also shown. To facilitate comparison between the schemes, each plot shown in Fig. 2 uses a resolution of $\zeta = 5°$. Table 1 includes the number of discrete points generated for each of the four schemes with resolutions of $\zeta = 2.5, 5$ and 10°. Fig. 3 shows oversampling plots for each scheme with a common resolution of $\zeta = 5°$. Histograms of the closest adjacent vector are shown in Fig. 4.
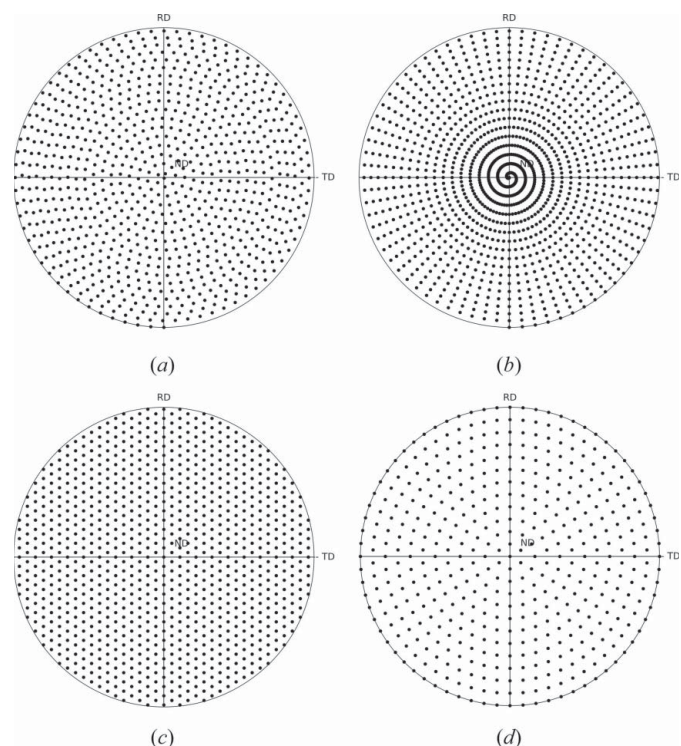
Figure 2
Discrete scatter plots of the sampling schemes, (*a*) the new DSS scheme, (*b*) the Holden spiral, (*c*) the Rizzie grid and (*d*) the Matthies hexagonal scheme. All are plotted on an equal area pole figure with axes x = rolling direction (RD), y = transverse direction (TD) and z = normal direction (ND). All plots use a scheme resolution of $\zeta = 5°$ and an equal area stereographic projection
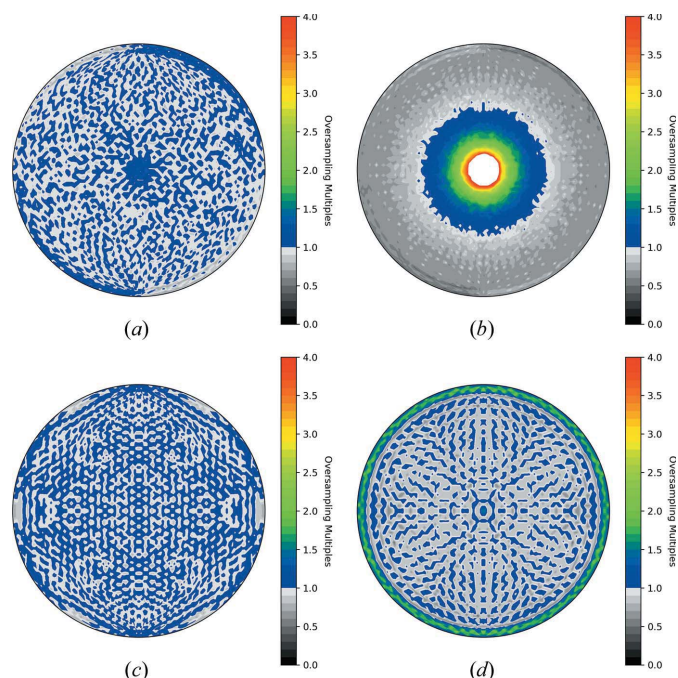
Figure 3
Filled contour plots of the sampling schemes, (*a*) the DSS, (*b*) the Holden spiral, (*c*) the Rizzie grid and (*d*) the Matthies hexagonal scheme. The color axes show the oversampling multiple (density of points).

As Figs. 2(*a*) and 3(*a*) show, the DSS scheme has an even distribution of points across the pole figure. The points are arranged as nearly concentric rings with an offset determined by ζ. The contour plot in Fig. 3(*a*) indicates slight oversampling along the ND and along the periphery of the pole figure (RD–TD plane) at the top right and bottom left. The periphery at the top left and bottom right was slightly undersampled. The over- and undersampling along the periphery is due to the proximity of the points to the $\chi = 90°$ boundary, which is a symmetry plane for the pole figure (Kington, 2015). If the points are close to this boundary, they represent an over-sampling, as shown by comparing Figs. 2(*a*) and 3(*a*). Table 1 shows that the DSS has fewer points than the Rizzie and Holden schemes but more than the Matthies scheme.

While the path of the Holden spiral is similar to that of the DSS, the rate at which the spiral completes one revolution is equal to the rate at which the spiral expands outwards. As shown in Fig. 2(*b*), the region along the ND is heavily clustered with sampling points, while the periphery of the scheme pole figure grid is more sparsely populated with sampling points. The oversampling plot in Fig. 3(*b*) demonstrates this oversampling quite visibly along the ND, with a maximum value of 10, exceeding the upper bound of the color range used for the plots in Fig. 3. At $\zeta = 5°$ the Holden spiral samples 1297 points (Table 1), a greater number than any other sampling scheme explored in this work.

The Rizzie grid [Fig. 2(*c*)] samples the pole figure in a column-like arrangement of sampling points moving left to right on the pole figure, as opposed to the nearly concentric rings of sampling seen on the spiral scheme grids in Figs. 2(*a*) and 2(*b*). Similar to the DSS shown in Fig. 3(*a*), the distribution of points for the Rizzie grid shown in Fig. 3(*c*) is fairly even across the entire pole figure. There are small areas of under-sampling at 60° incremental patches along the $\chi = 90°$ boundary of the pole figure, corresponding to an 'edge' of the hexagonal grid. As listed in Table 1, the Rizzie grid has more points than the DSS, but fewer than the Holden spiral.

The Matthies hexagonal scheme shown in Fig. 2(*d*) seems to blend concepts from both the spiral schemes and the Rizzie grid, adopting a concentric sampling pattern and a hexagonal arrangement of sampling points. However, the oversampling plot shown in Fig. 3(*d*) indicates an

Figure 4
Normalized histograms showing the relative probability distributions of the angle to the closest adjacent scattering vector for the sampling schemes, (*a*) the DSS, (*b*) the Holden spiral, (*c*) the Rizzie grid and (*d*) the Matthies hexagonal scheme. All plots use a scheme resolution of $\zeta = 5°$. Note the *y*-axis scales are dissimilar to show details of the distribution.

oversampling by a factor of 2 along the outer ring of the pole figure. This oversampling is probably due to the points on the outer ring lying on the $\chi = 90°$ boundary, which is a symmetry line between the upper and lower halves of the pole figures. The obvious advantage of this scheme is shown in Table 1, as the Matthies hexagonal scheme requires the lowest number of points of any scheme investigated, with approximately half as many points as the Rizzie grid and DSS.

The histograms shown in Fig. 4 provide additional details on the distribution of diffraction vectors. While each sampling scheme uses a common resolution parameter value of $\zeta = 5°$ in its construction, the range and distribution of values differ between the schemes. For the DSS shown in Fig. 4(a), the median value of this distribution is 5.0° with the distribution narrowly grouped at 5°. A few adjacent vectors with a smaller angle can be seen with low relative probability. The Holden spiral shown in Fig. 4(b) has a quite different distribution, with the relative probability initially sharply decreasing at smaller angles, but reaching a constant value between 3.0 and 0°. The median value of the Holden spiral is 3.5°. While the extent of the Rizzie hexagonal grid shown in Fig. 4(c) is comparable to that of the DSS, the Rizzie hexagonal grid has a wider spread near 5°, with a greater proportion of adjacent vectors smaller than 5°. The median value of the Rizzie hexagonal grid is 4.5°. The Matthies hexagonal scheme shown in Fig. 4(d) has a similar spread to the Rizzie grid, but the Matthies hexagonal scheme is biased towards larger values of adjacent vector angle. The median value for the Matthies hexagonal scheme is 6.0°. There is also a significant distribution of values at 0° for the Matthies hexagonal scheme, supporting the oversampling plot in Fig. 3(d) at $\chi = 90°$ values.

3.2. Comparison of ODF accuracy

The ODF reconstruction accuracy is shown in Table 2. The accuracy in ODF reconstruction was not greatly affected by the sampling scheme. The Holden spiral performed slightly worse than the other three schemes for the entire range of component half-widths. As expected, component half-widths that were smaller than or equal to the sampling scheme resolution of $\zeta = 5°$ (and reconstructed ODF resolution of 5°) have significant errors. At component half-widths greater than 30°, the errors approach zero as there is minimal texture in the ODFs. Thus, half-width values greater than 30° are not included in Table 2.

3.3. Comparison of phase fraction accuracy

The oversampling plots suggest there may be bias errors in the phase fraction due to some regions of the pole figures being measured with greater frequency than others. Fig. 5 shows the range of calculated phase fractions for each scheme. The range of phase fractions comes from calculations for all 91 (7×13) texture component combinations at each ODF half-width value. The scheme resolution ζ was held constant at 5° for each scheme. A 5% relative error bound on the phase fraction was used as a benchmark for 'tolerable' error, as done by Creuziger et al. (2018a). While ODF half-width values up to

Table 2
ODF error (mean difference) per sampling scheme and component half-width.

ODF error is caculated as an average for all components. Units are multiples of a uniform or random distribution. The data use a scheme resolution of $\zeta = 5°$ and reconstructed ODF half-width of 5°.

Component half-width	DSS	Holden	Rizzie	Matthies
2.5°	1.158	1.305	1.161	1.201
5.0°	0.235	0.321	0.235	0.238
10.0°	0.059	0.084	0.060	0.065
15.0°	0.045	0.069	0.046	0.049
20.0°	0.027	0.046	0.026	0.031
25.0°	0.025	0.032	0.025	0.027
30.0°	0.019	0.021	0.019	0.020

50° were investigated, the range of ODF half-widths plotted in Fig. 5 was reduced as the values converged at larger values of ODF half-width, similar to Table 2. This method of plotting does not preserve information on which texture components contribute most significantly to the variation. Heat maps of the phase fraction for each texture combination are available in the supporting information that accompanies this paper.

The ranges of texture-induced bias errors in the phase fraction calculation are comparable for the DSS and Rizzie grid schemes. For both, the ranges of bias errors are within the 5% relative error bounds for ODF half-widths greater than or equal to 5°. For the Matthies scheme, bias errors were nearly within a 5% relative error bound for ODF half-widths greater than or equal to 10°. The Holden spiral had errors that exceeded the 5% relative error bound until an ODF half-width of 30°.

Restating these observations in a different way, for the DSS scheme and Rizzie grid a scheme resolution of $\zeta = 5°$ was accurately able to measure phase fractions in materials with texture sharpness comparable to a half-width of 5°. For the Matthies grid, a scheme resolution of $\zeta = 5°$ was only able to
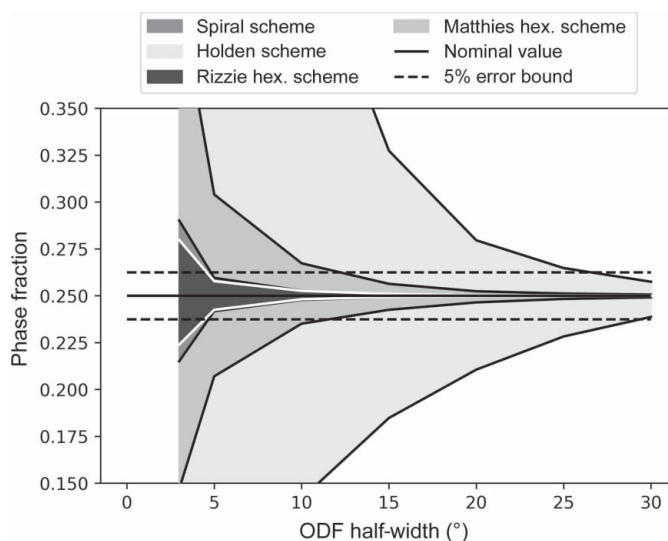
Figure 5
A comparison of the phase fraction error range for all four schemes. The scheme resolution was fixed at $\zeta = 5°$.

measure phase fractions accurately in materials with texture sharpness comparable to a half-width of 10°. Finally, the Holden spiral was only able to measure phase fractions accurately in materials with texture sharpness comparable to a half-width of 30°. Inspection of the experimental ODFs by Kocks *et al.* (1998), Dillamore & Roberts (1964), Bleck *et al.* (1991) and Kestens & Jonas (2005) indicates texture sharpnesses of the order of ODF half-widths of 5–20° are commonly encountered.

4. Discussion

The DSS scheme has successfully been demonstrated to have more even pole figure coverage than the other schemes explored, comparable phase fraction accuracy to the Rizzie hexagonal scheme and approximately 13% fewer points than the Rizzie hexagonal scheme. This phase accuracy is largely due to the dynamic nature of updating the angular increment as a function of tilt and not forcing each segment to reset at 0° on each rotation. In addition, unlike the Rizzie or Matthies schemes, the DSS can be run continuously, possibly allowing for additional data to be recorded while traversing the spiral. As Fig. 4 shows, the DSS has the tightest spread and a median value that matches ζ.

There are significant disadvantages to the Holden spiral scheme compared with the DSS. While they both share a fundamental spiral pattern, the DSS offers significant improvements in measurement accuracy and measurement time. Given their common origin, they both experience some level of uneven sampling along the ND and along the periphery of the pole figure, but this unevenness is much greater in the Holden spiral. As the ND orientation corresponds directly to many common texture orientations, there are several textures that affect the ability of this scheme to mitigate measurement error effectively.

Comparing the DSS and the Rizzie grid, both schemes nearly evenly cover the pole figure. The DSS shows slight oversampling along the ND compared with the Rizzie grid, while the Rizzie grid has a few regions of undersampling arranged in a 60° pattern along the periphery of the pole figure. These differences account for the slight differences in which texture components cause bias errors. As noted above, the DSS accomplishes even pole figure coverage with fewer measurement points than the Rizzie grid. The motor motion for the DSS is also more continuous than the Rizzie grid, which requires more motor oscillation to reach each prescribed tilt angle.

The Matthies hexagonal scheme has a strong advantage over the DSS in terms of the number of points required, as the Matthies hexagonal scheme samples nearly 50% fewer points than either the spiral scheme or the Rizzie hexagonal grid. However, the effective resolution of the Matthies hexagonal grid is 6°, as shown in Fig. 4(*d*), despite the use of a resolution parameter of $\zeta = 5°$. In addition, the Matthies hexagonal scheme oversamples along the periphery of the pole figure, resulting in more bias errors that are more significant than for the DSS or the Rizzie hexagonal scheme. This oversampling is

due to the points lying on the $\chi = 90°$ symmetry boundary. While locating the points along the RD–TD plane is advantageous for pole figure measurements, weighting these points by a factor of 0.5 relative to interior points or only measuring $\phi \leq 180°$ (due to sample symmetry) may improve accuracy for phase fractions.

Despite all four grids having a fixed scheme resolution ζ in this analysis, there are differences in the number of nearest neighbors and in the angular distance to neighboring points. The scatter plot for the Matthies grid [Fig. 2(*d*)] visually appears less dense than those of the spiral [Fig. 2(*a*)] and Rizzie hexagonal grid [Fig. 2(*c*)]. In general, the scheme resolution parameter does not match the actual distribution. As Table 2 shows, the ODF accuracy does not depend strongly on the scheme used, up to the resolution limit of the pole figure and/or ODF.

The Matthies hexagonal scheme has correspondingly larger phase fraction errors than the Rizzie hexagonal and DSS schemes, and phase fraction errors outside the error bounds for half-widths less than 10°. However, as many common rolling textures can be approximated by texture components with a half-width ranging from 10 to 20°, the advantage of fewer points may outweigh the decreased accuracy.

Reversing the criteria of scheme resolution and texture half-width, one can get an estimate of how sharp a texture a particular sampling scheme can resolve. In the cases of the DSS and Rizzie grids, the scheme resolution should be approximately half of the ODF half-width value. The texture literature currently offers little guidance on how best to assess whether an ODF is artificially 'smoothed' due to the pole figure resolution.

5. Conclusions

This paper has successfully demonstrated a new spiral scheme for conducting diffraction experiments. Compared with schemes currently in use, the new dynamically segmented spiral scheme has advantages in terms of evenness of pole figure coverage, number of points (time per measurement) and phase fraction accuracy. The phase fraction accuracy has been shown to be robust for a variety of texture components commonly encountered in steels and for texture sharpness exceeding what is commonly encountered for rolled sheet steels.

This scheme provides a promising alternative to conventional methods of simultaneous texture and phase fraction measurement and takes advantage of modern computer control no longer requiring mechanical linkages.

Research Center (ASPPRC) at the Colorado School of Mines for extending him an internship opportunity and the chance to contribute towards this project, specifically ASPPRC Director Dr John Speer and ASPPRC students and staff for their guidance, support and friendship; and to the BASIS Chandler High School Senior Project Program, specifically his counsellors and advisors, for supporting and advising him during the research period.

References

Abu-Farha, F., Hu, X., Sun, X., Ren, Y., Hector, L. G., Thomas, G. & Brown, T. W. (2018). *Metall. Mater. Trans. A*, **49**, 2583–2596.

Bleck, W., Großterlinden, R., Lotter, U. & Reip, C.-P. (1991). *Steel Res.* **62**, 580–586.

Brand, P. C., Prask, H. J. & Gnaeupel-Herold, T. (1997). *Physica B*, **241–243**, 1244–1245.

Bunge, H.-J. (1982). *Texture Analysis in Materials Science.* London: Butterworths.

Creuziger, A., Calhoun, C. A., Poling, W. A. & Gnäupel-Herold, T. (2018a). *J. Appl. Cryst.* **51**, 720–731.

Creuziger, A., Calhoun, C., Poling, W. & Gnäupel-Herold, T. (2018b). *DataSet: Assessment of Bias Errors Caused by Texture and Sampling Methods in Diffraction-Based Steel Phase Measurements*, https://github.com/usnistgov/Texture-Sampling-PhaseMeasurement-BiasErrors.

Creuziger, A., Phan, T. & Pagan, D. (2021). *J. Appl. Cryst.* **54**, 1480–1489.

De Moor, E., Gibbs, P. J., Speer, J. G., Matlock, D. K. & Schroth, J. G. (2010). *Iron Steel Technol.* **7**, 132.

Dillamore, I. L. & Roberts, W. T. (1964). *Acta Metall.* **12**, 281–293.

Fawcett, T. G., Needham, F., Faber, J. & Crowder, C. E. (2010). *Powder Diffr.* **25**, 60–67.

Han, H. N., Oh, C.-S., Kim, G. & Kwon, O. (2009). *Mater. Sci. Eng. A*, **499**, 462–468.

Hielscher, R. & Schaeben, H. (2008). *J. Appl. Cryst.* **41**, 1024–1037.

Holden, A. N. (1953). *Rev. Sci. Instrum.* **24**, 10–12.

International Organization for Standardization (2020). ISO 13067:2020, https://www.iso.org/standard/74309.html. Geneva: ISO.

Jatczak, C. F., Larson, J. A. & Shin, S. W. (1980). *Retained Austenite and its Measurements by X-ray Diffraction: An Information Manual.* Warrendale: Society of Automotive Engineers.

Kallend, J. S., Kocks, U. F., Rollett, A. D. & Wenk, H.-R. (1991). *Textures Microstruct.* **14**, 1203–1208.

Kestens, L. & Jonas, J. J. (2005). *Metalworking: Bulk Forming*, Vol. 14A, *Transformation and Recrystallization Textures Associated with Steel Processing*, pp. 685–700. Materials Park: ASM International.

Kington, J. (2015). *mplstereonet – Stereonets for matplotlib*, https://pypi.org/project/mplstereonet/.

Klug, H. P. & Alexander, L. E. (1974). *X-ray Diffraction Procedures.* New York: John Wiley & Sons Inc.

Kocks, U. F., Tomé, C. N. & Wenk, H.-R. (1998). *Texture and Anisotropy.* Cambridge University Press.

Larson, A. C. & Von Dreele, R. B. (2004). *GSAS.* Report LAUR 86-748. Los Alamos National Laboratory, New Mexico, USA.

Lutteroti, L. (2000). *Acta Cryst.* A**56**, s54.

Lutterotti, L., Chateigner, D., Ferrari, S. & Ricote, J. (2004). *Thin Solid Films*, **450**, 34–41.

Lutterotti, L., Matthies, S., Wenk, H.-R., Schultz, A. S. & Richardson, J. W. (1997). *J. Appl. Phys.* **81**, 594–600.

Madsen, I. C., Scarlett, N. V. Y., Cranswick, L. M. D. & Lwin, T. (2001). *J. Appl. Cryst.* **34**, 409–426.

Matthies, S., Pehl, J., Wenk, H.-R., Lutterotti, L. & Vogel, S. C. (2005). *J. Appl. Cryst.* **38**, 462–475.

Matthies, S. & Vinel, G. W. (1982). *Phys. Status Solidi B*, **112**, K111–K114.

Matthies, S. & Wenk, H.-R. (1992). *Phys. Status Solidi A*, **133**, 253–257.

Onuki, Y., Masumura, T., Tsuchiyama, T., Sato, S., Tomida, T. & Takaki, S. (2020). *Tetsu Hagane*, **106**, 457–464.

Peterson, N. E., Einhorn, J. R., Fancher, C. M., Bunn, J. R., Payzant, E. A. & Agnew, S. R. (2021). *J. Appl. Cryst.* **54**, 867–877.

Rizzie, A. C. (2008). *Math. Exch.* **5**, 10–17.

Roe, R. J. (1965). *J. Appl. Phys.* **36**, 2024–2031.

Rowles, M. R. (2021). *J. Appl. Cryst.* **54**, 878–894.

Schwartz, A. J., Kumar, M., Adams, B. L. & Field, D. P. (2009). Editors. *Electron Backscatter Diffraction in Materials Science.* Heidelberg: Springer.

Toby, B. H. & Von Dreele, R. B. (2013). *J. Appl. Cryst.* **46**, 544–549.

Vogel, S. C., Biwer, C. M., Rogers, D. H., Ahrens, J. P., Hackenberg, R. E., Onken, D. & Zhang, J. (2018). *J. Appl. Cryst.* **51**, 943–951.

Wenk, H.-R. (1991). *J. Appl. Cryst.* **24**, 920–927.

Wenk, H.-R., Lutterotti, L. & Vogel, S. (2003). *Nucl. Instrum. Methods Phys. Res. A*, **515**, 575–588.

Wenk, H.-R., Lutterotti, L. & Vogel, S. C. (2010). *Powder Diffr.* **25**, 283–296.

Wenk, H.-R., Matthies, S., Donovan, J. & Chateigner, D. (1998). *J. Appl. Cryst.* **31**, 262–269.

Wright, S. I., Nowell, M. M. & Bingert, J. F. (2007). *Metall. Mater. Trans. A*, **38**, 1845–1855.

Xu, P. G., Harjo, S., Ojima, M., Suzuki, H., Ito, T., Gong, W., Vogel, S. C., Inoue, J., Tomota, Y., Aizawa, K. & Akita, K. (2018). *J. Appl. Cryst.* **51**, 746–760.